Chemical Engineering Journal 443 (2022) 136434

Contents lists available at ScienceDirect

Chemical Engineering Journal

journal homepage: www.elsevier.com/locate/cej

Surface spinel and interface oxygen vacancies enhanced lithium-rich layered oxides with excellent electrochemical performances

Gaige Zhang [a,1], Min Chen [a,b,1,*], Caixing Li [a], Binhong Wu [a], Jiakun Chen [a], Wenjin Xiang [a], Xinyang Wen [a], Dehui Zhang [a], Guozhong Cao [c,*], Weishan Li [a,b,c]

[a] School of Chemistry, South China Normal University, Guangzhou 510631, China
[b] Engineering Research Center of MTEES (Ministry of Education), Research Center of BMET (Guangdong Province), Engineering Lab. of OFMHEB (Guangdong Province), Key Lab. of ETESPG (GHEI), and Innovative Platform for ITBMD (Guangzhou Municipality), South China Normal University, Guangzhou 510006, China
[c] Department of Materials Science and Engineering, University of Washington, Seattle, Washington 98195, United States

ARTICLE INFO

Keywords:
Lithium ion battery
Li-rich layered oxide
Oxygen vacancies
$Li_4Mn_5O_{12}$
Coulombic efficiency

ABSTRACT

Li-rich layered oxide (LLO) is one of the most promising cathode materials for high energy–density lithium ion battery (LIB) due to its capacity more than 250 mAh g^{-1}. However, the low initial Coulombic efficiency, large voltage decay and poor cycling stability caused by irreversible lattice oxygen releasing hinder its further development. The present work demonstrates that a surface layer of spinel $Li_4Mn_5O_{12}$ rich of interface oxygen vacancies in LLO (denote as SLLO) reduces the voltage decay and suppresses the irreversible release of oxygen. When SLLO was used as a cathode in LIBs, the initial Coulombic efficiency is improved from 83% to 97%, a high reversible capacity of 303 mAh g^{-1} at a rate of 0.1C, as well as a capacity retention of 88% at 0.3C at 200 cycles, and corresponding voltage decay is also mitigated. Characterization and calculation reveal that the enhanced performance is attributed to the rapid Li^+ extraction/insertion in the surface spinel; the irreversible release of O_2 is reduced through the interfacial oxygen vacancies; the adverse reaction is largely suppressed by spinel coating layer.

1. Introduction

Lithium ion batteries with higher energy density are essential for energy storage systems, especially for electric vehicles. Among many lithium-ion cathode materials, Li-rich layered oxide (LLO), $xLi_2MnO_3 \cdot (1\text{-}x)LiMO_2$ (M = Ni, Co and Mn), composed by the rhombohedral $LiMO_2$ structure with R-3 m space group and the monoclinic Li_2MnO_3 with C2/m space group, has attracted much attention due to its higher specific capacity (greater than250 mAh g^{-1}) than any of the commercially employed cathodes [1]. The extraordinary capacity of LLO comes from the traditional cationic redox in $LiMO_2$ component as well as the contribution of anionic redox from Li_2MnO_3. Typically, the anionic redox reaction concludes a reversible anodic redox (O^{2-} to O^{n-}) and an irreversible lattice oxygen loss (O^{2-} to O_2), the former can provide capacity while the latter brings about a series of problems such as the large initial irreversible capacity loss, poor structural stability and side reaction [2]. The release of O_2 would induce the migration of transition metal (TM) ion to neighboring Li slabs, resulting in the local phase transformation from a layered into spinel-like structure. Such distorted lattice in the defect spinel phase would hinder Li diffusion and result in a lower Li^+ coefficient [3].

To circumvent these issues, surface modification with metal oxides [4–7], fluorides [8–9] and phosphates coating [10–11] has been studied to stabilize LLO structure and suppress side reactions between LLO and electrolyte at high voltages. However, most coating materials are non-electrochemically active and their crystal structures are incompatible with LLO, reducing the capacity and limiting their further developments. It has been reported that leaching by strong acid like HNO_3 or H_2SO_4 largely limited the anionic activity and improved the initial Coulombic efficiency though LLO crystal structure was easily damaged, resulting in a quick decay of electrochemical performance [12–15]. Oxygen vacancy could also reduce the irreversible oxygen release and suppress the formation of unstable superoxides and the structural degradation. For example, Qiu et al. [1] reported that the release of O_2 in $Li_{1.144\text{-}2x}Ni_{0.136}Co_{0.136}Mn_{0.544}O_{2\text{-}x}$ has been largely reduced by a surface oxygen vacancy. Ma et al. [16] modelled and revealed that oxygen

* Corresponding authors.
E-mail address: gzcao@uw.edu (G. Cao).
[1] These authors contributed equally to this work.

https://doi.org/10.1016/j.cej.2022.136434
Received 1 February 2022; Received in revised form 8 April 2022; Accepted 13 April 2022
Available online 18 April 2022
1385-8947/Published by Elsevier B.V.

vacancies affect the coordination of Mn and enhance the structural stability. Pei et al. [17] showed that the oxygen vacancies could trap O-O dimers through the reductive coupling and enhance the reversibility of anion redox. However, single oxygen vacancy could not yield a solid protection and cannot support long-term cycling. Spinel phase with a good structural compatibility with LLO has been introduced to coat LLO and it was demonstrated to suppress the anionic redox and improve the Li^+ diffusion. For example, $LiMn_2O_4$-like spinel phase doped in $Li_{1.2}Mn_{0.54}Ni_{0.13}Co_{0.13}O_2$ exhibited an improved initial Coulombic efficiency from 67% to 75%, but with serious Mn dissolution [18]. $LiNi_xMn_{2-x}O_4$, $Li_xTM_{3-x}O_4$ and $Li_4Mn_5O_{12}$ were further developed to suppress lattice O loss and Mn dissolution [19–21]. Among them, $Li_4Mn_5O_{12}$ spinel has less lattice mismatch with the bulk layered structure and higher oxidation state of Mn^{4+}, which is in favor of Li^+ transport, the inhibition of Jahn-Teller distortion and the dissolution of Mn [22]. Mn^{4+} in the $Li_4Mn_5O_{12}$ spinel phase only can be reduced to $Mn^{3.4+}$ rather than Mn^{3+} [23]. Introducing oxygen vacancy to LLO with spinel coating layer would suppress the release of O_2 and maintain the structural integrity, but how to simply add both into LLO is still big challenging.

In this work, we integrated LLO with $Li_4Mn_5O_{12}$ outlayer and interfacial oxygen vacancies (SLLO) via a universal oxalic acid assisted delithiation process. Characterizations and calculations revealed that the $Li_4Mn_5O_{12}$ spinel phase originated from the Li_2MnO_3 component of LLO via H^+/Li^+ exchange and subsequent a heat-treated process, and oxygen vacancies were mainly in the layer/spinel interface. SLLO demonstrated a higher initial Coulombic efficiency of 97% than LLO of 83%. The product with 7.5% $Li_4Mn_5O_{12}$ coating layer and 4.7% interface oxygen vacancy (SLLO-2) exhibits the best cycling stability and rate capability. The electrochemical impedance spectroscopy (EIS) results reveal that the lithium ion diffusion coefficient has been enhanced with $Li_4Mn_5O_{12}$ coating layer and oxygen vacancy. The characterizations of SLLO-2 electrode after cycling show that $Li_4Mn_5O_{12}$ as a good coating layer largely suppresses the side reaction and maintains the structural stability. The first-principle calculations indicate that the covalency between TM and oxygen and the density of the state of O 2p band decrease, and local spin density of Mn near interface oxygen vacancy increases and then can act as a redox buffer for anionic oxidation. Ex-gas chromatography (GC) and differential electrochemical mass spectrometry (DEMS) display that the interface oxygen vacancies can largely reduce the release of irreversible O_2 loss. This work provides a new strategy to quantitatively compose high performance LLO with layer/spinel heterostructure and oxygen vacancy for the next generation high energy density cathode.

2. Experimental section

2.1. Material synthesis

$Mn(CH_3COO)_2{\cdot}4H_2O$, $Co(CH_3COO)_2{\cdot}4H_2O$ and $Ni(CH_3COO)_2{\cdot}4H_2O$ with concentration of 2.0 M was mixed in the ethylene glycol; then NH_4HCO_3 solution was added dropwise under vigorously stirring for 1 h; finally, the sealed Teflon ware was put into a stainless steel autoclave and hold at 180 °C for 10 h. The resulting pink precipitates $(Mn_{0.67}Co_{0.17}Ni_{0.17})CO_3$ were centrifuged and dried at 80 °C and then calcined at 500 °C for 5 h. The synthesized oxide precursor was mixed with $LiOH{\cdot}H_2O$ and sintered at 800 °C for 12 h to get Li-rich layered oxide material (LLO).

To prepare the layer/spinel Li-rich material (denoted as SLLO), For SLLO-1, 0.1 g $C_2H_2O_4$ was dissolved in 60 mL ultra-pure water and after that 0.5 g LLO was dispersed in the above solution with stirring for 30 min. For SLLO-2, the acid leaching time was prolonging to 60 min. For SLLO-3, leaching time was similar to SLLO-2, but the concentration of $C_2H_2O_4$ was double. In order to explore where the spinel phase originate from, we also used the similar method to prepare Li_2MnO_3 and $LiNi_{1/3}Co_{1/3}Mn_{1/3}O_2$ respectively, and treat them with the same molar concentration of oxalic acid for the same time and 500 °C sintering in air.

2.2. Material Characterization

Scanning electron microscopy (SEM, FEI Quanta 250 FEG) and transmission electron microscopy (TEM, FEI Talos F200X), high resolution TEM (HRTEM) and corresponding fast Fourier transform (FFT) were utilized to demonstrate the morphologies and structures of samples. EDS (TEAM PV6300) was used to detect the contents and distribution of various elements. Inductively coupled plasma optical emission spectroscopy (ICP-OES, SPECTRO ARCOS MV) was used to investigate the metal elements ratio in the as-obtained samples. The pore structure and specific surface areas of as-prepared sample were characterized by means of N_2 sorption isotherms with Gold APP instrument and calculated by Brunauer-Emmett-Teller (BET) method. The X-ray diffraction (XRD, Rigaku UltimalV, Japan) was carried out to analyze the structure information at a scanning rate of 3° min^{-1} from 10° to 80°. The Rietveld refinements of lattice constants, atomic occupancies and phase constituents were performed by the Fullprof software package, where R-3 m phase with higher symmetry was applied to simplify the lattice parameters. Raman scattering was executed to determine the phase structure in a Raman spectrometer (WITec alpha 300R, Ulm, Germany) using 532 nm wavelength laser. The fitting results are according to Gauss peak function. X-ray photoelectron spectroscopic (XPS, AXIS SUPRA) was performed to characterize the chemical environment and valent state. XPS PEAK 4.1 soft was used to fit peaks. Thermogravimetric analysis (TGA) was carried out on a PerkinElmer TGA at a heating rate of 10 °C min^{-1} in flow air from room temperature to 800 °C. The Differential Scanning Calorimeter (DSC) measurement was conducted to probe the thermal stability with a PerkinElmer 4000 thermal analyzer from the ambient of 30 to 350 °C at a ramp rate of 10 °C min^{-1}. Electron paramagnetic resonance (EPR) measurement was conducted to determine the content of oxygen vacancy by a Bruker EMXPLUS instrument with a modulation frequency of 100 KHz. GC (9890A, China) measurement was utilized to detect the releasing gaseous compositions from V-type cells. The DEMS experiment was conducted according to our previous reports [24].

2.3. Electrochemical measurements

The cathode electrode slurry was prepared by mixing active materials (LLO and SLLO), acetylene black and PVDF with a weight ratio of 8:1:1 in N-methyl pyrrolidone and casted on aluminum foil. After drying at 120 °C for 12 h in a vacuum oven, the electrode was cut into disks of 12 mm diameter. The prepared cathode and lithium metal anode, separator (Celgard 2300) and the electrolyte with 1 M $LiPF_6$ in a mixture of EC, DEC and EMC (EC: DEC: EMC = 3:2:5 in weight) were assembled CR2025 coin cells in a glovebox under an argon atmosphere. All cells were aged 12 h before testing. The charge–discharge tests were performed on a Land CT 2001A testing system (Wuhan, China) in the voltage range between 2.0 and 4.65 V at the 25 °C with different current densities. Before cycling in 0.3C and 1C (1C = 200 mAh g^{-1}), the cells

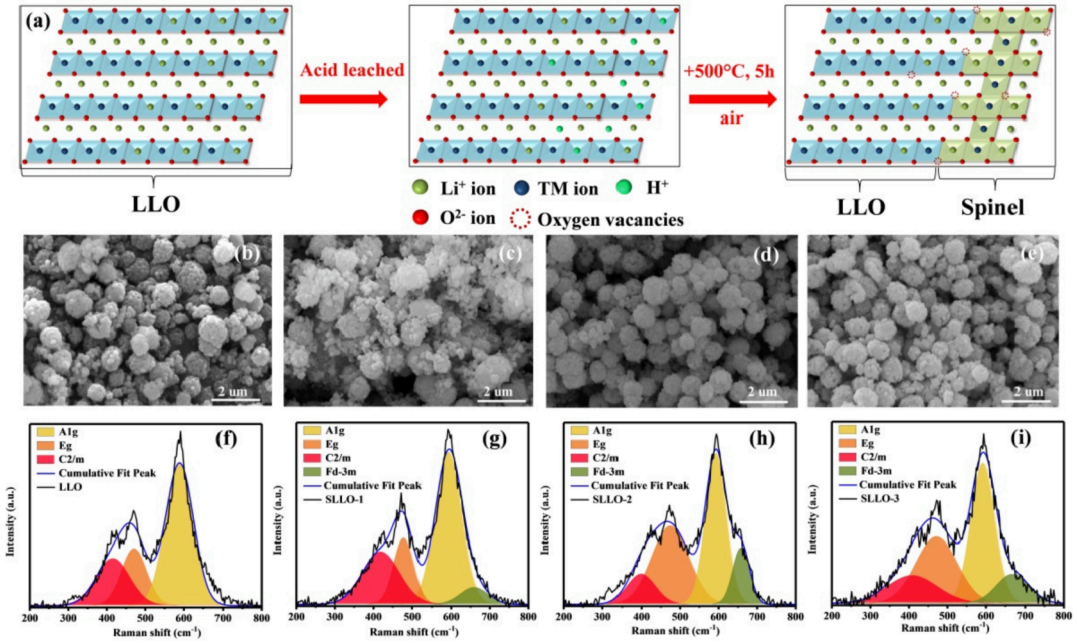

Fig. 1. (a) Schematic diagram of the acid leached interface engineering. SEM images of (b) LLO, (c) SLLO-1, (d) SLLO-2 and (e) SLLO-3. Raman spectra and the fitting results of (f) LLO, (g) SLLO-1, (h) SLLO-2 and (i) SLLO-3.

were activated at 0.1C for three cycles. The electrochemical impedance spectroscopy (EIS) was measured using an electrochemical workstation (PGSTAT-30) in the frequency range from 100 kHz to 0.01 Hz. The V-type cells were charged to 4.8 V at 0.1 mV s^{-1} scan rate and keep 20 h at 4.8 V.

2.4. Computation method

The first-principles calculations based on the Density Functional Theory (DFT) were performed using the CASTEP [25]. The Perdew-Burke-Ernzerhof (PBE) exchange–correlation functional [26] within the generalized gradient approximation (GGA) was employed to describe the exchange–correlation energy. The projector-augmented-wave (PAW) [27] method was adopted for the pseudopotentials. The energy cutoff for the plane wave basis expansion was set to 450 eV. The primitive cell of $Li_5Mn_7O_{16}$ (Fd-3 m with spinel structure) and $2 \times 2 \times 1$ supercell of $Li_7CoNiMn_3O_{12}$ (R-3 m with layered structure) were used, and a vacuum region of 10 Å above $Li_5Mn_7O_{16}$/$Li_7CoNiMn_3O_{12}$ (layer/spinel structure) slab was used to ensure the decoupling between neighboring systems. The geometry optimizations were performed until the forces on each ion was reduced below 0.01 eV $Å^{-1}$, and the Monkhorst-Pack k-point [28] sampling was set to $5 \times 5 \times 5$, $5 \times 5 \times 3$ and $5 \times 5 \times 1$ for $Li_5Mn_7O_{16}$, $Li_7CoNiMn_3O_{12}$ and $Li_5Mn_7O_{16}$/$Li_7CoNiMn_3O_{12}$, respectively. The van der Waals interaction has been considered using the Grimme dispersion scheme [29]. To improve the description of electronic structures, DFT + U approach has been employed, with U = 3.10 eV, 3.40 eV and 3.40 eV for Mn, Co and Ni based on early publications [30].

3. Results and discussion

Fig. 1a schematically illustrated the formation of SLLO: (1) the exchange of surface Li^+ with H^+ in oxalate acid, and (2) the removal of H_2O and O_2 at 500 °C heat-treatment, accompanied by the formation of

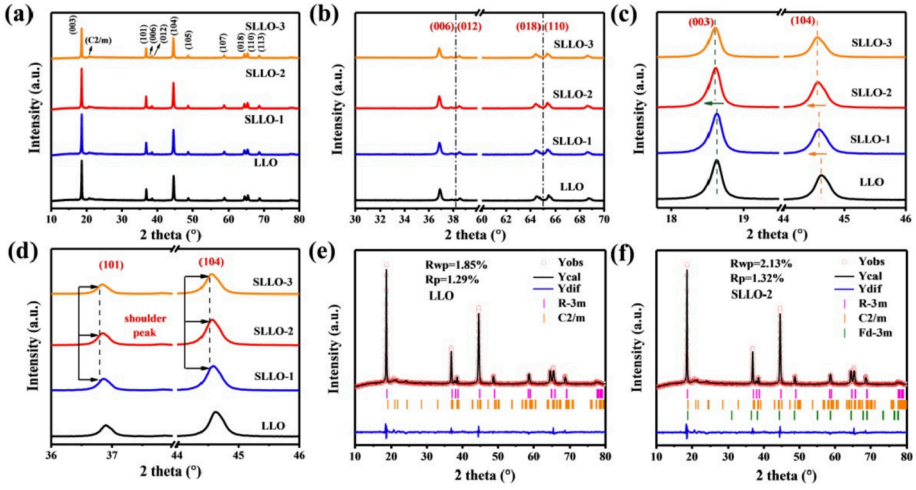

Fig. 2. (a) XRD patterns of the as-obtained samples, (b) the magnified splitting pair peaks of (006)/(012) and (018)/(110), (c) the magnified (003) and (104) diffraction peaks, (d) the shoulder peaks of SLLO. Riveted refinement results of (e) LLO and (f) SLLO-2.

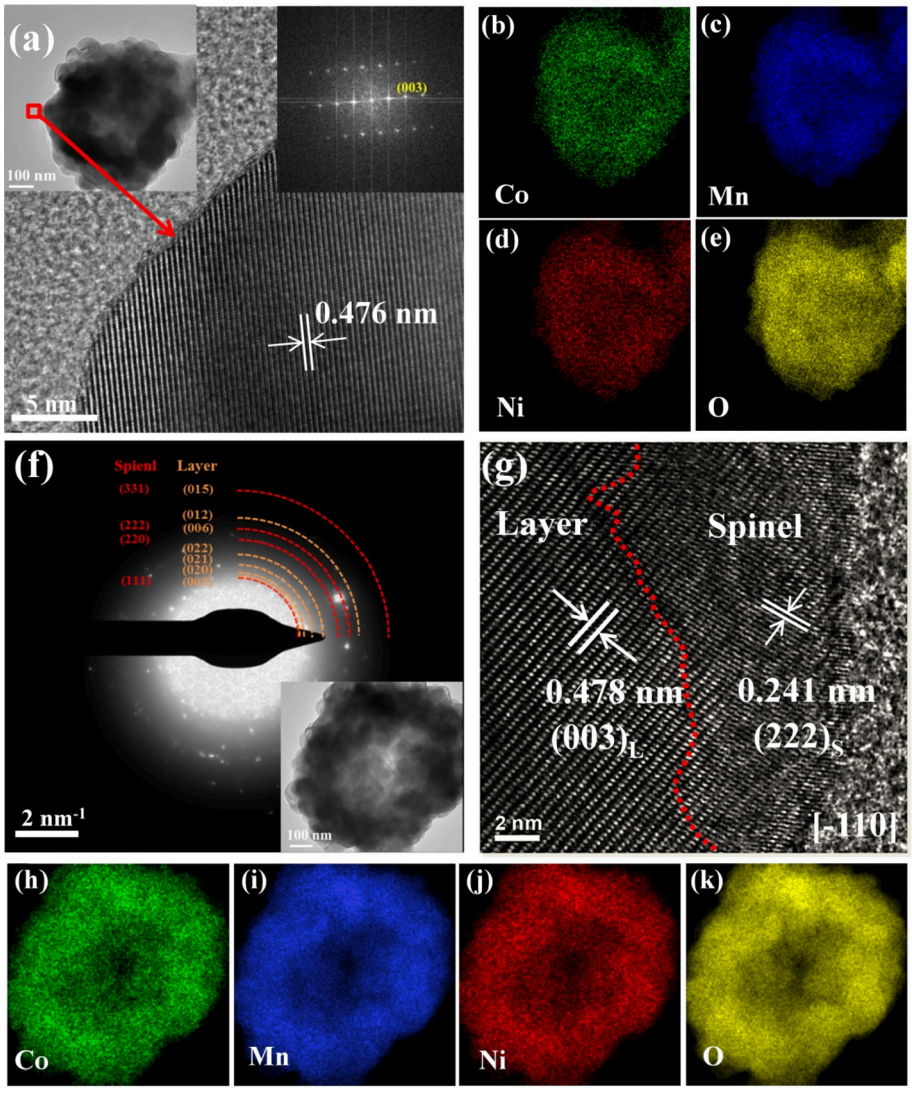

Fig. 3. (a) HRTEM image, (b-e) elements mapping of Co, Mn, Ni and O in LLO. (f) TEM image and corresponding polycrystalline SAED patterns of SLLO-2, (g) HRTEM image of SLLO-2, (h-k) elements mapping of Co, Mn, Ni and O in SLLO-2.

surface spinel phase and oxygen vacancies. In order to clarify where Li^+ ions is exchanged in step 1, so two phases (Li_2MnO_3 and $LiMn_{1/3}Ni_{1/3}Co_{1/3}O_2$) in LLO do the same treatment with oxalate acid. XRD patterns in Fig. S1**a-b** show the structure of $LiNi_{1/3}Co_{1/3}Mn_{1/3}O_2$ remained the same and (003) peak position does not shift, revealing no appreciable variation of interplanar space. While for Li_2MnO_3 in Fig. S1**d-e**, (002) peak shift to a smaller angle, suggesting lattice constant has changed. The Raman spectrum of $LiNi_{1/3}Co_{1/3}Mn_{1/3}O_2$ in Fig. S1**c** also exhibits the vibration mode remained unchanged but a shoulder appeared at 651 cm^{-1} for Li_2MnO_3 in Fig. S1**f**. This shoulder is a typical A_{1g} vibration in spinel phase [7]. The above results and following XPS demonstrate that the spinel phase is likely formed possibly through the following reactions:

Fig. 1d-e show that all samples have a good porous micro-nano morphology, the primary particles are densely stacked and composed of large secondary particles. The average second particle size is about 1–2 μm, which inherits from the $(Mn_{0.67}Co_{0.17}Ni_{0.17})CO_3$ precursor (Fig. S2). As shown in Fig. S3, the BET surface area is 6.4 $m^2\ g^{-1}$ and 8.3 $m^2\ g^{-1}$ for LLO and SLLO-2. The N_2 absorption–desorption isotherms in Fig. S3 a-b present a hysteresis loop between desorption and adsorption for both samples, revealing the characteristic of porous structure. The pore size distribution curves in Fig. S3 c-d exhibit the hierarchical porous structure with pore distributed from 1 nm to 120 nm for both sample. SLLO-2 demonstrates larger pore volume with more aggregated pore size at around 10 nm. The EDS line scanning in Fig. S4 displays that TM elements are distributed uniformly across the microspheres and the atomic ratio of Mn, Ni and Co are close to theoretical ratio. The ICP-OES results (Table S1) show that TM elements have not changed but Li

$$Li_2MnO_3 \xrightarrow[Exchange]{H^+} Li_{2-x}H_xMnO_3 \xrightarrow[500^\circ C]{Loss H_2O and O_2} (1-\frac{5}{6}X)Li_2MnO_3@\frac{x}{6}Li_4Mn_5O_{12}+\frac{\delta}{2}O_2+O(v)+\frac{\delta}{2}H_2O \quad (1)$$

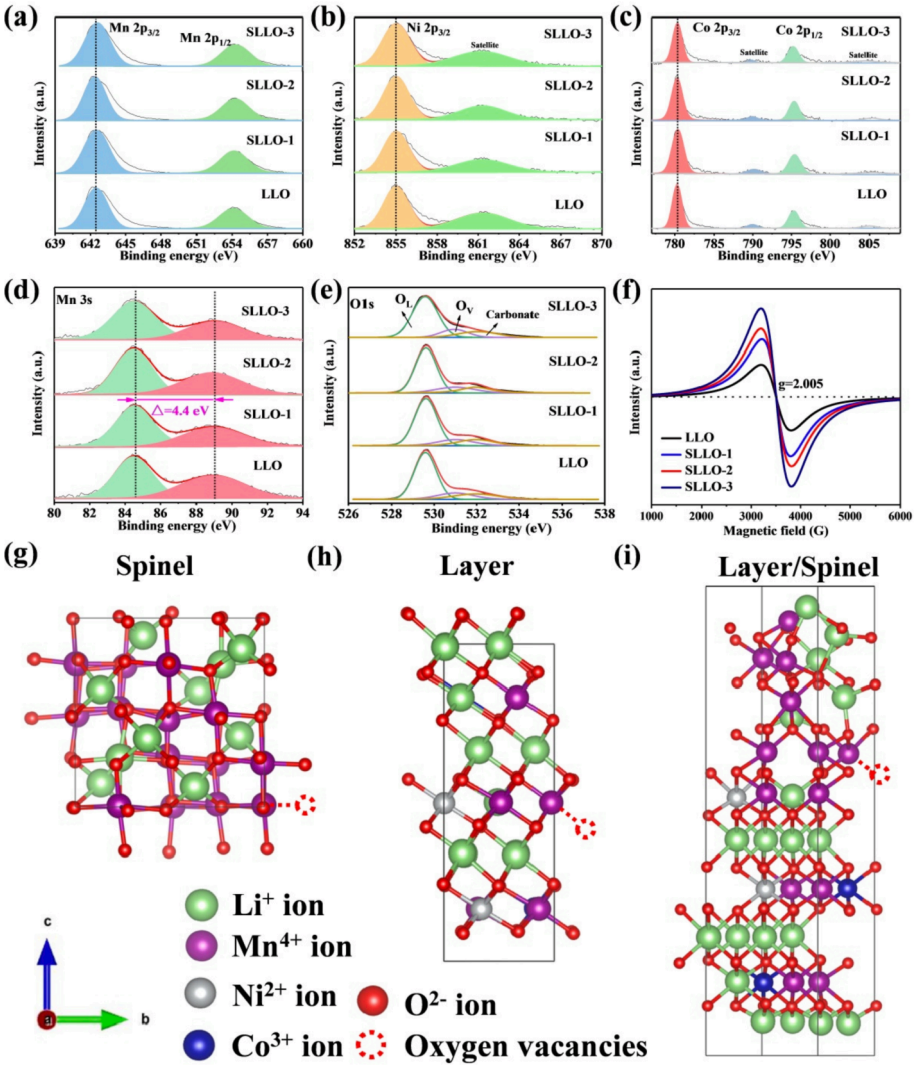

Fig. 4. XPS spectra of (a) Mn 2p, (b) Ni 2p, (c) Co 2p, (d) Mn 3 s, and (e) O 1 s for the as-obtained samples. (f) Room temperature EPR spectra of the as-obtained samples. Structure models of (g) the spinel structure with Fd-3 m ($Li_5Mn_7O_{16}$), (h) the layered structure with R-3 m ($Li_7CoNiMn_3O_{12}$), and (i) the layer/spinel structure ($Li_5Mn_7O_{16}$@$Li_7CoNiMn_3O_{12}$).

decreased, which is attributing to the exchange Li^+ with H^+.

The Raman spectra in Fig. 1f-i show typical vibration features of LLO: the peak positions of the yellow region around 600 cm^{-1} and 480 cm^{-1} correspond to M−O stretching (A_{1g}) mode and O-M−O bending (E_g) mode of R-3 m structure, the red peak areas at 410 cm^{-1} are assigned to the presence of Li_2MnO_3 (space group: C2/m) [31], indicating that the layered structure of the modified samples is well maintained and this is in good agreement with the XRD results. A shoulder band at 650 cm^{-1} appearing in SLLO is ascribed to the Mn-O stretching vibrations in $Li_4Mn_5O_{12}$ spinel phase with Fd-3 m space group [7]. After fitting, the spinel phase in SLLO-1, SLLO-2 and SLLO-3 are estimated to be approximately 4.9%, 7.5% and 11%.

XRD patterns in Fig. 2a show all samples have narrow and sharp peaks, indicating good crystallinity. All strong peaks are well indexed to a rhombohedral phase with R-3 m structure, and several weak peaks between 20° and 25° could be attributed to a monoclinic Li_2MnO_3 phase with C2/m space group [32]. The clear splitting of (0 0 6)/(0 1 2), (0 1 8)/(1 1 0) pair peaks in Fig. 2b reveal that all the samples have a good layer structure, which indicate the main structure of SLLO has not changed. As shown in Fig. 2c, the peak intensity ratio of I(0 0 3)/I(1 0 4) is 1.59 for LLO and 1.55 for SLLO-2, respectively, which reveals that both sample have low Li/TM mixing [33]. As shown in Fig. 2c, (0 0 3) and (1 0 4) peaks of modified samples are left-shifted implying that the lattice expansion, which may be attributed to more TM ions occupying the lithium slabs due to the existence of spinel phase. Fig. 2d shows shoulder peaks on the left of (1 0 1) and (1 0 4) peaks of SLLO sample, which can be ascribed to the formation of spinel phase with cubic close-packed oxygen stack [21]. The refined results display in Fig. 2e,f and Table S3, Table S4. The weight fraction of R-3 m structure in LLO and SLLO-2 exhibits no significant differences, while C2/m structure in SLLO-2 reduces to 33.50%, compared with 41.36% in LLO. In addition, the newly formed of spinel Fd-3 m phase is 7.5% in SLLO-2, which is almost equal to the reduced C2/m structure and further suggests that the spinel phase is mainly converted from Li_2MnO_3 phase. The lattice parameters of LLO are a = 2.84 Å, and c = 14.19 Å, while a = 2.84 Å, and c = 14.20 Å for SLLO-2. The expansion of c indicates the surface spinel phase may bring about oxygen vacancy via sharing O atom [18]. Both of the c/a ratio for the hexagonal unit cell of the pristine LLO (4.996) and SLLO-2 (5.000), respectively, indicating the layered bulk structure has not been much changed but the heterojunction interfaces induced by surface spinel phase is full of vacancies [34], which been confirmed by oxygen occupancy in the refined results (Table S4). Specifically, the amount of oxygen vacancies in the LLO and SLLO-2 samples were determined to 2.4% and 4.7%, respectively.

The inset images in Fig. 3a,f reveal that two samples exhibit uniform hollow microspherical structure. TEM-EDS shown in Fig. 3b-e, h-k

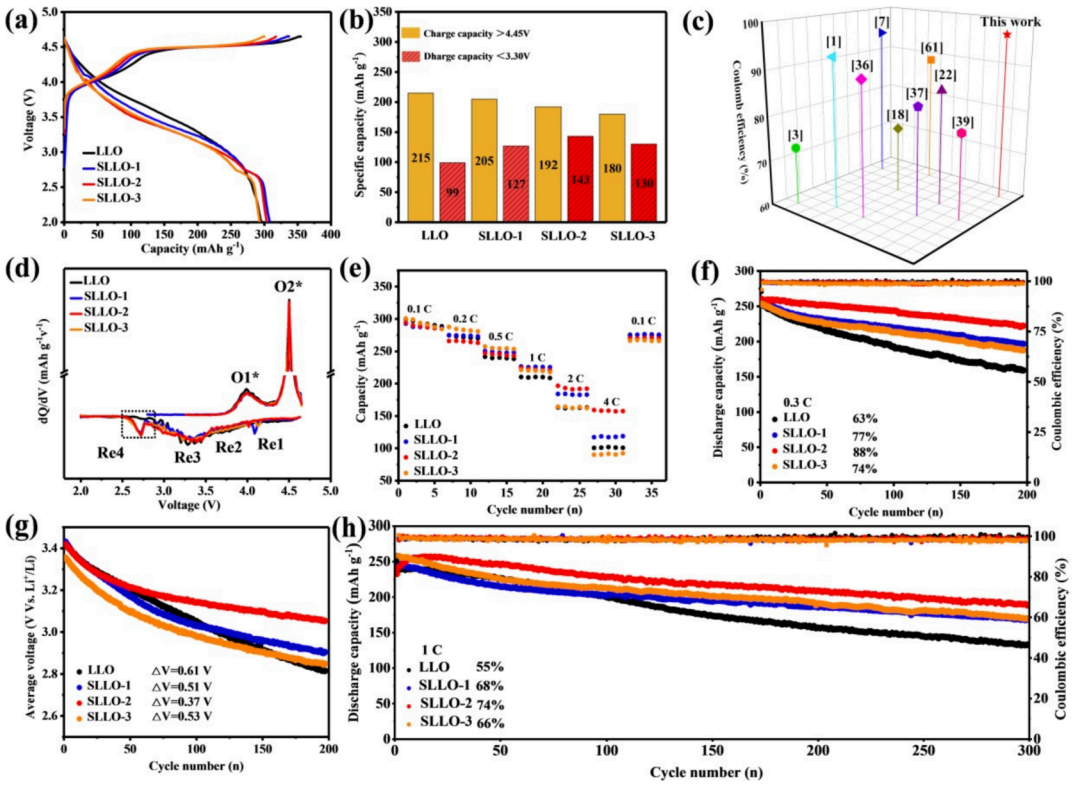

Fig. 5. Electrochemical performances of the as-obtained electrode. (a) Initial charge–discharge curves at 0.1C, 2.0–4.65 V, (b) capacity contribution above 4.45 V and under 3.3 V, (c) comparison of the initial Coulombic efficiency of our work and other reports, (d) corresponding dQ/dV profiles, (e) the rate capability, (f) the cycling stability and corresponding Coulombic efficiency at 0.3C, (g) the plots of average discharge voltage vs. cycles, (h) the cycling performance and corresponding Coulombic efficiency at 1C.

reveals that Co, Ni, Mn and O distributed uniformly in both samples. The spacing of the lattice planes are 0.476 nm for LLO (Fig. 3a), which is attributed to (003) spacing in the layered structure in corresponding FFT image [35]. The selected area electron diffraction (SAED) of SLLO-2 in Fig. 3f shows the second particle is polycrystalline and its electron diffraction rings contain layered and spinel characteristics, in which four diffraction rings is well indexed to (111), (220), (222) and (331) planes of Fd-3 m spinel phase and the remained rings belong to the layered (R-3 m and C2/m) phase [36]. HRTEM images along the [−110] zone axis in Fig. 3g exhibits the spinel phase coating layer with thickness of 5–10 nm is well integrated at the surface of SLLO-2. In the layered/spinel heterostructure, a lattice spacing of 0.478 nm represents (003) plane in hexagonal $LiMO_2$ layered phase while a d-spacing of 0.248 nm corresponds to (222) plane in cubic $Li_4Mn_5O_{12}$ spinel phase [22]. The enhanced (003) spacing of SLLO-2 sample might be attributed to the presence of spinel phase and oxygen vacancy with larger electrostatic repulsion [37].

The XPS survey spectra were exhibited in **Fig. S5**, Mn 2p, Ni 2p, Co 2p, Mn 3 s and O 1 s spectra were presented in Fig. 4a-e. The spectra of transition metals and oxygen showed no shift of the peak positions within pristine LLO and SLLO. The dominant peaks of 2p at binding energies of 642.3, 845.3 and 780.5 eV represent Mn^{4+}, Ni^{2+} and Co^{3+} in both LLO and SLLO [33]. Typically, the distance between the two peaks of Mn 3 s has been used to approximate the average oxidation state (AOS) by the equation [38]:

$$AOS = 8.956–1.126\triangle E. \quad (2)$$

The fitting analysis of Mn 3 s spectra reveals that there is Mn^{4+} at the surface for LLO and SLLO. According to the above results, the surface oxidation states of Ni/Co/Mn in SLLO have not been influenced by the spinel structure, which further demonstrates that the spinel structure in SLLO should belong to the $Li_4Mn_5O_{12}$-type.

In Fig. 4e, all the O1s spectra display three distinct characteristic peaks at near 529.2 eV, 531 eV and 532 eV, which is corresponding to the lattice oxygen (M−O), the O state in the oxygen vacancy and the carbonate species [39–40]. From the XPS result fitting and acid alkali titration experiment (Table S5), the surface carbonate species are almost the same in LLO and SLLO sample. **Fig. S6** shows the proportion of oxygen vacancy increased with the increase of the formed spinel phase, which reveals the spinel phase is favorable to generate oxygen vacancy. Fig. 4f presents the pristine and modified samples exhibit a sharp EPR signal at g-factor 2.005, showing the presence of oxygen vacancies in LLO and SLLO [41]. It is found that the oxygen vacancies concentration is increased with the increase of spinel phase (Table S6), which is consistent with the XPS and XRD results. As oxygen vacancies can be filled with oxygen, thereby the sample with oxygen vacancies will loss less weigh at high temperatures [42]. As shown in TG curve (**Fig.S7**), the first weight loss region around 100 °C is attributed to adsorption and H_2O, while the second weight loss from 450 °C to 800 °C is corresponding to lattice oxygen escaping and decomposing of carbonate species. The less weight loss of SLLO-2 might be attributable to oxidation at elevated temperature with oxygen vacancies filled.

Fig. 4g-i exhibits the structure model with oxygen vacancies, where one oxygen vacancy is formed in the spinel, layer and layer/spinel interface. The formation energies of oxygen vacancy were calculated by the following formulas:

$$E_{form} = E(vacancy) - E(pure) + \mu(O) \quad (3)$$

Where E(pure) is the total energy of the represent model of spinel ($Li_5Mn_7O_{16}$), layer ($Li_7CoNiMn_3O_{12}$), and $Li_5Mn_7O_{16}/Li_7CoNiMn_3O_{12}$. E (vacancy) is the total energy of the above structure with oxygen vacancy and $\mu(O)$ is the chemical potentials of O atom. Regarding the location of oxygen vacancies, three models were calculated, in which one of the lowest energy was regarded as the most optimized position [43]. For

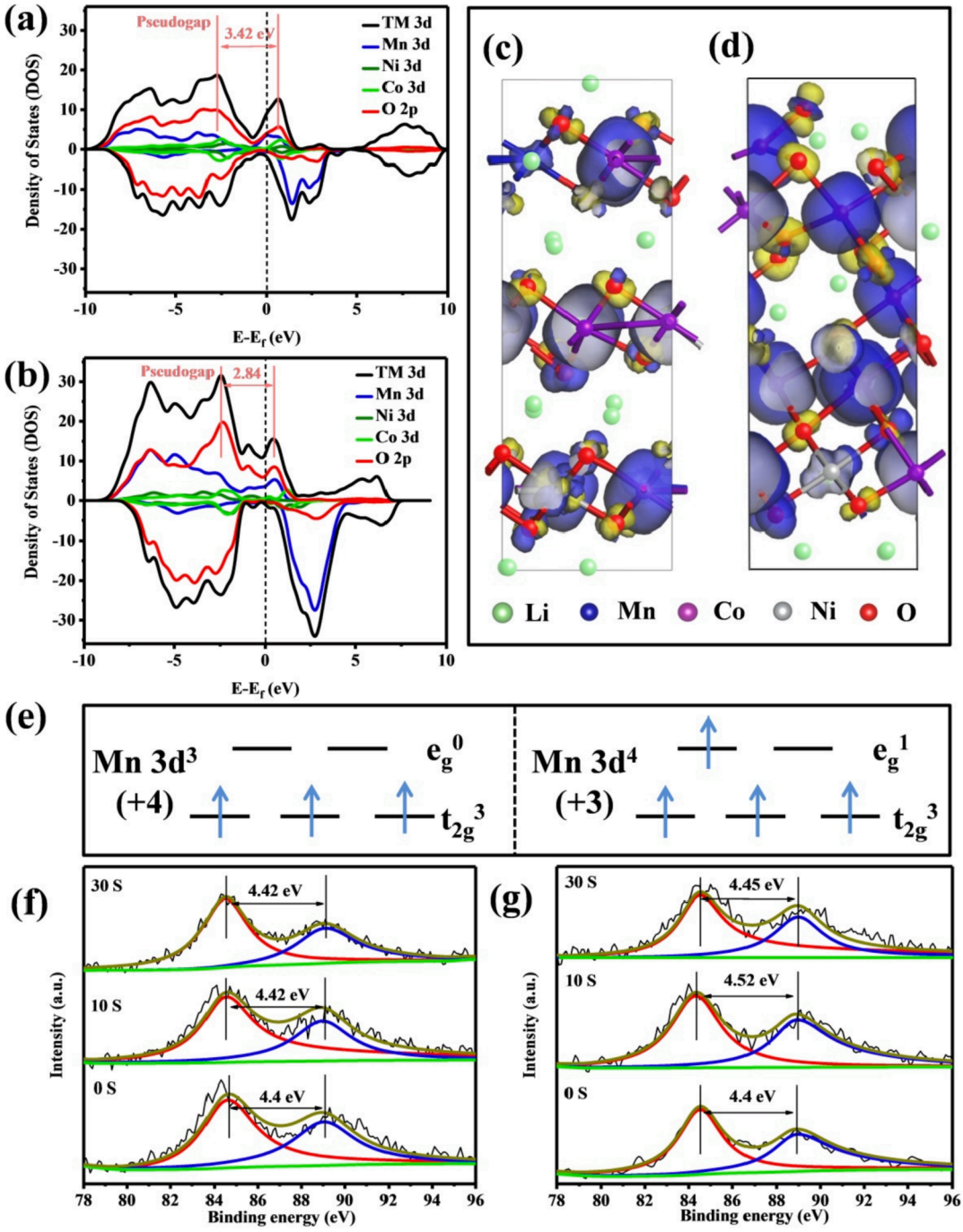

Fig. 6. (a, b) The projected density of states (pDOS) and (c,d) spin density differences of (a, c) LLO, (b, d) SLLO-2. The up- and down-spin electrons are in yellow and blue, respectively, (e) schematic diagram of 3d orbitals electronic state of Mn. XPS in-depth patterns for Mn of (f) LLO and (g) SLLO-2.

$Li_5Mn_7O_{16}$ (Fd-3 m) (Fig. 4g), the energy barrier of oxygen migration is calculated to be about 2.63 eV. However, as for the $Li_7CoNiMn_3O_{12}$ (R-3 m) (Fig. 4h), the oxygen migration energy barrier increases to 3.17 eV, indicating the more difficult oxygen migration than spinel phase. While, for $Li_5Mn_7O_{16}/Li_7CoNiMn_3O_{12}$ heterostructure (Fig. 4i), the oxygen migration energy barrier decreased to 2.36 eV, which reveal that the oxygen vacancy is more easily to occur at their interface [17]. Compared with layered structure, the spinel phase with 3D Li^+ diffusion channels exhibits excellent Li^+ diffusion kinetics. Interface oxygen vacancies would hinder the outward migration of oxygen anions, and maintain structural integrity and improve reversible capacity [44].

Fig. 5a displays the initial charge/discharge profiles of LLO and SLLO. All of them show a similar lithium insertion/extraction behavior, consisting of a slope and a plateau region. The slope region below 4.45 V is mainly attributed to the oxidation reactions of cationic ions, the plateau region at around 4.45 V is associated with the Li^+ further extraction from the TM layer with oxygen anion oxidation [45]. In Fig. 5b, the capacities at 4.45 V decrease from 215, to 205, 192, and 180 mAh g^{-1} for LLO, SLLO-1, SLLO-2 and SLLO-3 respectively, indicating less lattice oxygen releasing in SLLO [46,47]. The initial discharge capacities of the LLO, SLLO-1, SLLO-2 and SLLO-3 are 295, 307, 303 and 293 mAh g^{-1}, and the Coulombic efficiency is 83%, 91%, 94% and 97%, respectively, which is attributed to highly reversible anionic redox in SLLO [46]. For comparison, the initial Coulombic efficiency results for other modifications such as only oxygen vacancies [1,7], only spinel phase coating [3,18,22,36,37,39,61] are also included in Fig. 5c. It can

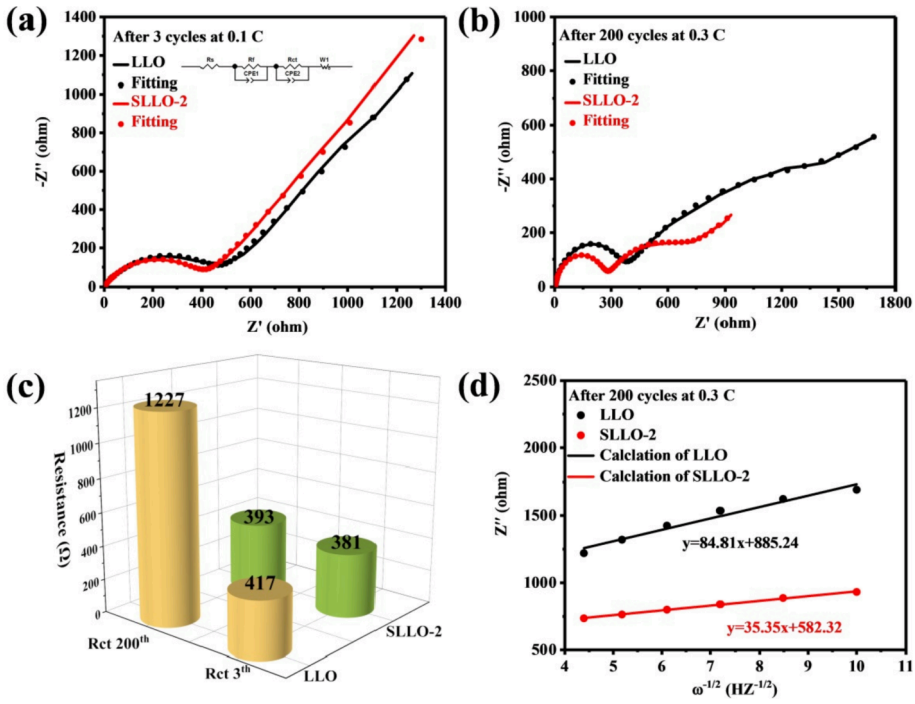

Fig. 7. (a) Nyquist plots of the electrodes and the corresponding equivalent circuit (inset) after 3cycles at 0.1C, (b) EIS spectra of electrode after 200 cycle at 0.3C, (c) the fitting results of the 3cycles and 200 cycles, (d) the relationship plot between Z'' and $\omega^{-1/2}$ derived from the low frequency region of the corresponding electrochemical impedance spectra.

be seen that this work integrated both oxygen vacancies and $Li_4Mn_5O_{12}$ greatly improves the reversibility of anionic redox. The gas evolution has been conduct by V-type cell and detected by GC. As shown in **Fig. S8a-d**, the electrolyte levels of before and after charging in SLLO-2 has less change than LLO, suggesting less gas generation for SLLO-2 [48]. GC (**Fig. S8e**) demonstrates that the main components of the gas are oxygen and carbon oxides. The oxygen comes from the irreversible lattice oxygen releasing from LLO and SLLO, while the carbon oxides come from the decomposition of electrolyte. Compared with LLO, SLLO-2 releases less oxygen and carbon oxides during charging. The DEMS results in **Fig. S9** also verify the O_2, CO_2 and CO evolution in SLLO-2 is mitigated. The discharge capacity below 3.3 V of SLLO (127 mAh g^{-1} for SLLO-1, 143 mAh g^{-1} for SLLO-2 and 130 mAh g^{-1} for SLLO-3) is higher than the LLO (99 mAh g^{-1}), which is attributed the characteristic Mn^{4+} reduction, and is relative to excess Li^+ insertion into the empty 16c octahedral sites of spinel $Li_4Mn_5O_{12}$ [49]. As shown in differential charge and discharge curves (Fig. 5d), the first oxidation peak about in the 3.8 V is the oxidization of cationic ions. The very strong oxidation peak (around 4.45 V) could be attributed to the oxidation of lattice oxygen. Three peaks appear in discharge profiles for all samples: Re1 at 4.45 V is related to the reduction of oxygen anions, Re2 at 3.8 V is the reduction of Ni^{4+}/Ni^{2+} and Co^{4+}/Co^{3+}, Re3 at 3.4 V is attributed to the reduction of Mn^{4+}/Mn^{3+} [50]. Comparing with the pristine sample, a new reduction peak Re4 at 2.8 V (black rectangle in Fig. 5d) is observed in SLLO, attributing to the insertion of Li^+ accompanied with Mn^{4+} reduction [51–52]. The corresponding integral areas of Re4 from SLLO-1 to SLLO-2 increase while for SLLO-3, it decreases, which is ascribed to the lower theoretical capacity of $Li_4Mn_5O_{12}$ spinel phase [18,24]. The best content of the spinel phase is estimated to be approximately 7.5%.

As shown in Fig. 5e, the SLLO samples enhance the rate capability and improve the capacity recovery after high rate cycles. At the rate of 4C, the capacity of SLLO-2 is 158 mAh g^{-1}, larger than 101 mAh g^{-1} in the LLO. Fig. 5f shows that SLLO-2 delivers a highest capacity of 253 mA g^{-1} and exhibits the best cycle performance at 0.3C after 200 cycles with capacity retention of 88%, compared to 63% for LLO, 77% for SLLO-1 and 74% for SLLO-3. After 200 cycles at 0.3C, the discharge capacity of SLLO-2 maintained at 222 mA g^{-1} higher than that of the LLO (159 mAh g^{-1}), SLLO-1 (197 mAh g^{-1}), and SLLO-3 (188 mAh g^{-1}). The Coulombic efficiency in SLLO is higher and more stable. As shown in Fig. 5g, the average discharge voltage decay of LLO is about 0.61 V (3.1 mV per cycle), SLLO-1 is about 0.51 V (2.5 mV per cycle), and SLLO-3 is about 0.53 V (2.6 mV per cycle), while for SLLO-2 is only 0.37 V (1.8 mV per cycle) after 200 cycles, which indicates that SLLO can well suppress voltage decay thus keep the structure integrity. As shown in **Fig. S10a,c**, SLLO-2 electrode shows obviously less capacity decline and voltage decay than the LLO from the 50 cycles to 200 cycles. In **Fig. S10b,d**, the overlap of dQ/dV curves among different cycles for LLO is worse than SLLO-2, indicating the more serious electrochemical reaction reversibility. It is worth noting that with the cycle number increase, the voltage of Re3 peak for LLO shifts from 3.3 V to 2.7 V, while from 3.0 V to 2.9 V for SLLO-2. According previous reports, Re3 move towards to lower potential is mainly ascribed to the transition from the layered structure to defect spinel structure, which always caused by the initial irreversible oxygen loss [37]. As for LLO, there are more oxygen release than SLLO-2, thus more TM ions migrated into the Li ion vacancies to form amorphous spinel phase and continuous decrease the value of Mn^{4+} to Mn^{3+}. Jahn-Teller distortion of Mn^{3+} would further lead manganese dissolution and break the structure integrity [22]. However, these phenomena are largely suppressed by the $Li_4Mn_5O_{12}$ coating layer and their interface oxygen vacancies for the sample of SLLO, which have been confirmed by the following XPS and TEM results after cycling. As shown in Fig. 5h, the discharge capacities at 1C of the LLO and SLLO-2 samples are 240, 256 mAh g^{-1}, with capacity retention of 55%, 74% after 300 cycles. DSC was applied to evaluate the alleviated loss of lattice oxygen after modification. It can be seen from **Fig. S11** that the main of the exothermic peak for charged LLO at 195 °C while the SLLO-2 rises to 202 °C. The heat generation is reduced from 192 J g^{-1} to 139 J g^{-1} for LLO and SLLO-2, suggesting better thermal stability for the SLLO-2, which is due to less irreversible anion redox [53].

Density of states (DOS) and spin density differences (SDD) LLO and SLLO-2 with one oxygen vacancies were calculated and the results are shown in Fig. 6. The projected density of states (pDOS) plots of two

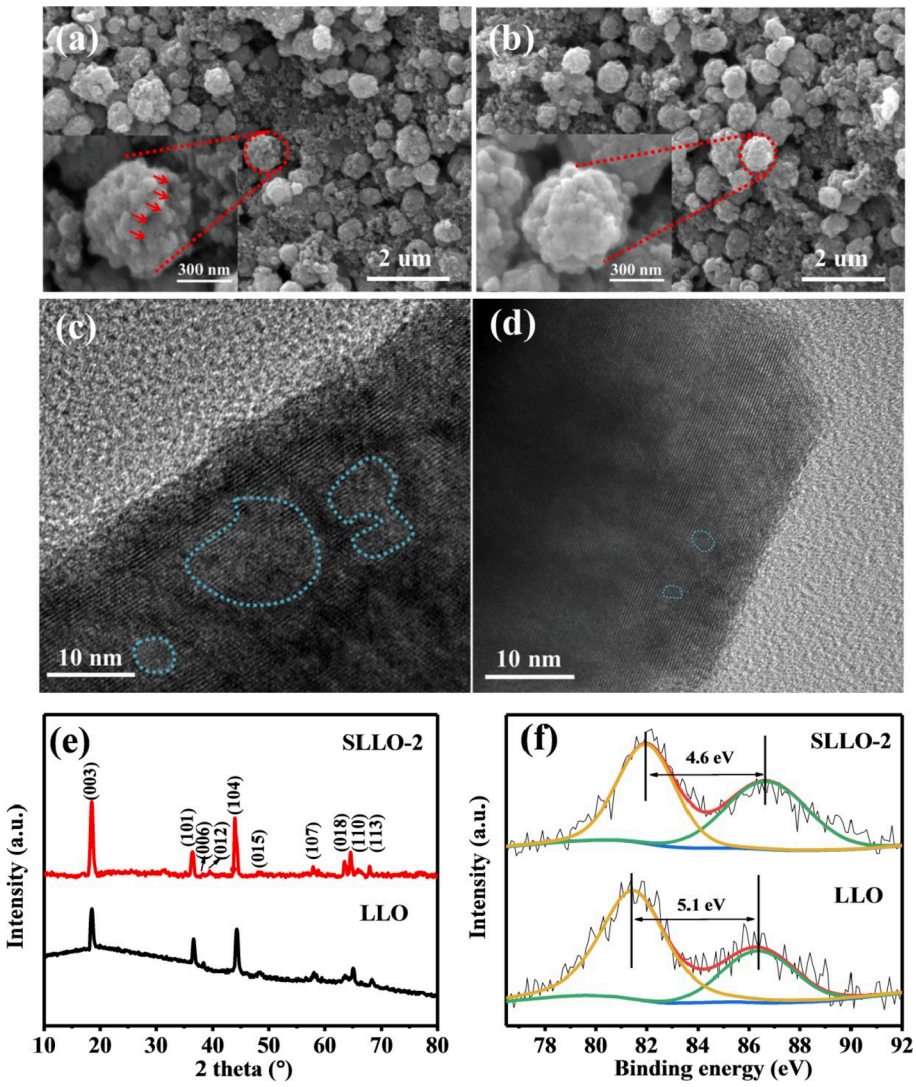

Fig. 8. Electrodes after 300 cycled at 1C, SEM images of (a) LLO and (b) SLLO-2, HRTEM images of (c) LLO and (d) SLLO-2, (e) XRD patterns and (f) XPS spectra of Mn 3 s.

samples was further performed to get the outline of their electronic structure. The corresponding results in Fig. 6a, b reveal that the electrical conductivity of LLO and SLLO-2 with oxygen vacancy has been improved when compared with the literatures without any modification because there are some obvious electron density of TM 3d and oxygen 2p in the vicinity of the Femi energy [40]. In addition, the pseudogap in LLO is 0.58 eV broader than SLLO-2 and the overlap between TM 3d and O 2p in LLO is more than SLLO-2. This phenomenon indicates that TM-O in SLLO-2 has lower covalence [54], which will alleviate charge compensation of anionic O [55]. When compared with the SDD (Fig. 6c, d) of Ni, Co and Mn in two samples near oxygen vacancies, it observes significant difference (more blue) of Mn, which means that the local electrons environment of Mn-O has been changed with interface oxygen vacancy [56]. According to calculated results, the difference between majority spin (up) and minority spin (down) in SLLO-2 is larger than LLO, indicating more unpaired electrons near Mn of SLLO-2. As for the the 3d orbitals electronic state of Mn in TMO_6 octahedral structure (Fig. 6e), Mn^{3+} with more unpaired electrons than Mn^{4+}, indicating the valence of Mn will decrease near oxygen vacancies, which is confirmed by the following XPS depth profile. In Fig. 6f,g, LLO and SLLO-2 are etched according to the depth of spinel phase in TEM. As for LLO, the valence state of Mn still maintains as the surface with etching time from 0 s to 30 s. While for SLLO-2, when etching at 10 s the valence state of Mn is reduced to + 3.87, and then reverts to + 3.95 at 30 s, which is attributed to the existence of rich interfacial oxygen vacancies, making local manganese coordination environments being changed. Such unpaired electrons can act as a buffer for charge compensation [57], which is in good agreement with the initial electrochemical performances.

Fig. 7 displays EIS plots after different cycles. In the Nyquist plot, they all contain one or two semicircles and a slop line, which can be well fitted by the equivalent circuit (embedded in Fig. 7a). The small interrupt in the Z' axis corresponds to the Ohmic resistance of the cell (Rs), a semicircle at the high frequency represents the solid electrolyte interface (SEI) film resistance (Rf) and a semicircle at medium frequency region is associated with charge transfer resistance (Rct), when the values of CPE1 and CPE2 are close, two semicircles will be merged to one pressed semicircle (as shown in Fig. 7a), the slope line in the low frequency region relates to Warburg impedance [58]. Based on above fitting, the simulated electrochemical parameters shown in Table S7 demonstrate that LLO and SLLO-2 exhibit similar impedance after 3cycles (Fig. 7a) at 0.1C. The Rct values of LLO and SLLO-2 cells are 417 and 381 Ω, respectively. However, in Fig. 7b, after 200 cycles at 0.3C the Rct value of LLO is 1227 Ω, much larger than SLLO-2 of 393 Ω, implying that the spinel phase can improve Li^+ diffusion and suppress structure evolution. The diffusion coefficients of lithium ions in LLO and SLLO-2 electrodes can be evaluated from the following equation and all constant is

described as previous reports [34,18]:

$$D_{Li}^{+} = R^2T^2/(2n^4A^2F^4C^2\sigma^2) \quad (4)$$

After calculation, the diffusion coefficient was 1.0×10^{-13} cm^2 s^{-1} for SLLO-2 electrode at 200 cycles, which is higher than that of 3.0×10^{-14} cm^2 s^{-1} for LLO electrode. Also, the lower Rf of SLLO-2 may be attributed to the stable electrode/electrolyte interface originated from $Li_4Mn_5O_{12}$ coating layer, which can decrease manganese dissolution and Jahn-Teller distortions. It is informed that the $Li_4Mn_5O_{12}$ spinel phase and oxygen vacancies on the SLLO-2 can suppress phase transition, accelerate lithium ion transmission, which is consistent with the high capacity retention as demonstrated by the cycling tests.

SEM image after cycled in Fig. 8a shows the broken secondary particles of the LLO sample with electrolyte corrosion. In Fig. 8b, the SLLO-2 sample exhibits intact porous micro-nano structure and no obvious cracks, which is ascribed to the protecting effects of spinel phase and the presence of oxygen vacancies. HRTEM images (Fig. 8c) show obvious defects (marked by blue lines) in the LLO, which could be attributed to an intermediate structure from layered structure to defect spinel phase [59], while SLLO-2 maintains its layered structure (Fig. 8d). XRD patterns after cycled in Fig. 8e reveal that (0 1 8)/(1 1 0) diffraction peaks of LLO disappear, while SLLO-2 remains with splitting. The peak splitting in XPS spectra (Fig. 8f) for LLO and SLLO-2 is 5.1 and 4.6 eV, so the average Mn oxidation states are + 3.21 and + 3.77 [38], respectively. The valence state of Mn also demonstrates that the surface of LLO is transformed into defect spinel phase, while SLLO-2 is maintained most $Li_4Mn_5O_{12}$ spinel phase. Compared to the defect spinel phase, the $Li_4Mn_5O_{12}$ can mitigate Jahn-Teller effect and suppress TM dissolution, thus reduce the reactions between electrode and electrolyte. As shown in the P 2p spectra (**Fig. S12a**) and F1s spectra (**Fig. S12b**) of the electrodes after cycling, Li_xPF_y (134.5 eV), $Li_xPO_yF_z$ (136.5 eV) and LiF (685.5 eV) are related to the $LiPF_6$ hydrolysis [39,60]. The O1s spectra in **Fig. S12c** consisted of M−O, and solution decomposition species of C = O and C-O [61]. The larger M−O peak and less C = O and C-O peaks in SLLO-2 indicate that the dissolution of transition metals and the carbonate solvents decomposition species is largely suppressed. From these results, it reveals that the decomposition of the lithium salt in two samples is less obvious than the solvent. The most likely reason is that the irreversible oxygen evolution species are easier to oxidize the carbonate solvents [62].

4. Conclusions

The introduction of surface $Li_4Mn_5O_{12}$ spinel layer and oxygen vacancies into LLO (SLLO) via H^+/Li^+ exchange and subsequent a heat-treated process has been demonstrated an efficient way to reduce the voltage decay and the irreversible release of oxygen. The LLO with 7.5% $Li_4Mn_5O_{12}$ and 4.7% interface oxygen vacancies (SLLO-2) demonstrated a superior electrochemical performance with initial Coulombic efficiency of 94%, and 88% capacity retention at 0.3C after 200 cycles. The improved electrochemical performance of SLLO is likely attributed to (1) good transport properties of surface $Li_4Mn_5O_{12}$ layer, and (2) better stability of the surface layer against oxygen erosion, and (3) interface oxygen vacancies regulating the local Mn-O interaction to suppress the irreversible oxygen evolution.

Declaration of Competing Interest

The authors declare that they have no known competing financial interests or personal relationships that could have appeared to influence the work reported in this paper.

Acknowledgement

This work is supported by National Natural Science Foundation of China (Grant No. 21872058 and No. 22109047), National Key Research and Development Project (Grant No. 2018YFE0124800) and Foundation for Young Teacher (Grant No. 20KJ20) and International Training Program for Young Talents of Guangdong Province.

Appendix A. Supplementary data

Supplementary data to this article can be found online at https://doi.org/10.1016/j.cej.2022.136434.

References

[1] B. Qiu, M. Zhang, L. Wu, J. Wang, Y. Xia, D. Qian, H. Liu, S. Hy, Y. Chen, K. An, Y. Zhu, Z. Liu, Y.S. Meng, Gas-solid interfacial modification of oxygen activity in layered oxide cathodes for lithium-ion batteries, Nat. Commun. 7 (2016) 12108.
[2] J. Lee, J.K. Papp, R.J. Clement, S. Sallis, D.H. Kwon, T. Shi, W. Yang, B. D. McCloskey, G. Ceder, Mitigating oxygen loss to improve the cycling performance of high capacity cation-disordered cathode materials, Nat. Commun. 8 (2017) 981.
[3] D. Luo, G. Li, C. Fu, J. Zheng, J. Fan, Q. Li, L. Li, A new spinel-layered Li-rich microsphere as a high-rate cathode material for Li-ion batteries, Adv. Energy Mater. 4 (2014) 1400062.
[4] M. Xu, Z. Chen, H. Zhu, X. Yan, L. Li, Q. Zhao, Mitigating capacity fade by constructing highly ordered mesoporous Al_2O_3/polyacene double-shelled architecture in Li-rich cathode materials, J. Mater. Chem. A 3 (26) (2015) 13933–13945.
[5] F. Wu, Z. Wang, Y. Su, N. Yan, L. Bao, S. Chen, $Li[Li_{0.2}Mn_{0.54}Ni_{0.13}Co_{0.13}]O_2$–$MoO_3$ composite cathodes with low irreversible capacity loss for lithium ion batteries, J. Power Sources 247 (2014) 20–25.
[6] B. Qiu, J. Wang, Y. Xia, Z. Wei, S. Han, Z. Liu, Enhanced electrochemical performance with surface coating by reactive magnetron sputtering on Lithium-rich layered oxide electrodes, ACS Appl. Mater. Interfaces 6 (12) (2014) 9185–9193.
[7] R. Yu, X. Zhang, T. Liu, L.I. Yang, L. Liu, Y.U. Wang, X. Wang, H. Shu, X. Yang, Spinel/layered heterostructured lithium-rich oxide nanowires as cathode material for high-energy Lithium-ion batteries, ACS Appl. Mater. Interfaces 9 (47) (2017) 41210–41223.
[8] Y.-K. Sun, M.-J. Lee, C.S. Yoon, J. Hassoun, K. Amine, B. Scrosati, The role of AlF_3 coatings in improving electrochemical cycling of Li-enriched nickel-manganese oxide electrodes for Li-ion batteries, Adv. Mater. 24 (9) (2012) 1192–1196.
[9] S. Pang, Y. Wang, T. Chen, X. Shen, X. Xi, D. Liao, The effect of AlF_3 modification on the physicochemical and electrochemical properties of Li-rich layered oxide, Ceram. Int. 42 (4) (2016) 5397–5402.
[10] J. Cho, Y.W. Kim, B. Kim, J.G. Lee, B. Park, A breakthrough in the safety of lithium secondary batteries by coating the cathode material with $AlPO_4$ nanoparticles, Angew. Chem. 42 (2003) 1618–1621.
[11] S.-H. Kang, M.M. Thackeray, Enhancing the rate capability of high capacity $xLi_2MnO_3{\cdot}(1-x)LiMO_2$ (M=Mn, Ni, Co) electrodes by $LiNiPO_4$ treatment, Electrochem. Commun. 11 (4) (2009) 748–751.
[12] C.S. Johnson, J.-S. Kim, C. Lefief, N. Li, J.T. Vaughey, M.M. Thackeray, The significance of the Li_2MnO_3 component in 'composite' $xLi_2MnO_3{\cdot}(1-x)LiMn_{0.5}Ni_{0.5}O_2$ electrodes, Electrochem. Commun. 6 (10) (2004) 1085–1091.
[13] S.H. Kang, C.S. Johnson, J.T. Vaughey, K. Amine, M.M. Thackeray, The effects of acid treatment on the electrochemical properties of $0.5Li_2MnO_3{\cdot}0.5LiNi_{0.44}Co_{0.25}Mn_{0.31}O_2$ electrodes in Lithium cells, J. Electrochem. Soc. 153 (2006) A1186.
[14] C.S. Johnson, N. L, C. Lefief, J.T. Vaughey, M.M. Thackeray, Synthesis, characterization and electrochemistry of lithium battery electrodes: x $Li_2MnO_3{\cdot}(1-x)$ $LiMn_{0.333}Ni_{0.333}Co_{0.333}O_2$ ($0 \leq x \leq 0.7$), Chem. Mater. 20 (2008) 6095-6106.
[15] K. Fujimoto, Y. Kitajima, A. Aimi, Effect of chemical oxidation of spinel-type $LiNi_{0.5}Mn_{1.3}Ti_{0.2}O_4$ by soaking in HNO_3, HCl and H_2SO_4, J. Solid. State. Chem. 302 (2021), 122366.
[16] Q.X. Ma, Z.J. Chen, S.W. Zhong, J.X. Meng, F.L. Lai, Z.F. Li, C. Cheng, L. Zhang, T. F. Liu, Na-substitution induced oxygen vacancy achieving high transition metal capacity in commercial Li-rich cathode, Nano Energy 81 (2020), 105622.
[17] Y. Pei, Q. Chen, M. Wang, B. Li, P. Wang, G. Henkelman, L. Zhen, G. Cao, C.Y. Xu, Reviving reversible anion redox in 3d-transition-metal Li rich oxides by introducing surface defects, Nano Energy 71 (2020), 104644.
[18] M. Chen, D.R. Chen, Y.H. Liao, X.X. Zhong, W.S. Li, Y.G. Zhang, Layered Lithium-rich oxide nanoparticles doped with spinel phase: acidic sucrose-assistant synthesis and excellent performance as cathode of Lithium ion battery, ACS Appl. Mater. Interfaces 8 (2016) 4575–4584.
[19] D. Lu, J. Li, J. He, R. Zhao, Y. Cai, Relationships between Structure, Composition, and Electrochemical Properties in LiNi x Mn 2– x O 4 [x = 0.37, 0.43, 0.49, 0.52, and 0.56] Spinel Cathodes for Lithium Ion Batteries, J. Phys. Chem. C 123 (14) (2019) 8522–8530.
[20] M. Zhang, Z. Li, L. Yu, D. Kong, Y. Li, B. Cao, W. Zhao, J. Wen, F. Pan, Enhanced long-term cyclability in Li-rich layered oxides by electrochemically constructing a $Li_xTM_{3-x}O_4$-type spinel shell, Nano Energy 77 (2020), 105188.
[21] J. Zhao, R. Huang, W. Gao, J.M. Zuo, X.F. Zhang, S.T. Misture, Y. Chen, J. V. Lockard, B. Zhang, S. Guo, M.R. Khoshi, K. Dooley, H. He, Y. Wang, An ion-

exchange promoted phase transition in a Li-excess layered cathode material for high-performance lithium ion batteries, Adv. Energy Mater. 5 (2015) 1401937.
[22] X.F. Bian, Q. Fu, H.L. Qiu, F. Du, Y. Gao, L.J. Zhang, B. Zou, G. Chen, Y.J. Wei, High performance $Li(Li_{0.18}Ni_{0.15}Co_{0.15}Mn_{0.52})O_2@Li_4M_5O_{12}$ heterostructured, Chem. Mater. 27 (2015) 5745–5754.
[23] Y. Lee, T.-H. Kim, Y.-K. Kwon, J. Shin, E. Cho, Selective formation of the $Li_4Mn_5O_{12}$ surface spinel phase in sulfur-doped Li-excess-layered cathode materials for improved cycle life, ACS Sustain. Chem. Eng. 8 (21) (2020) 8037–8048.
[24] M. Chen, G.G. Zhang, B.H. Wu, M.Z. Liu, J.K. Chen, W.J. Xiang, W.S. Li, N-Doped Graphene-Modified Li-Rich Layered $Li_{1.2}Mn_{0.6}Ni_{0.2}O_2$ Cathode for High-Performance Li-Ion Batteries, ACS Appl. Energy Mater. (2022), https://doi.org/10.1021/acsaem.Ic03936).
[25] S.J. Clark, M.D. Segall, C.J. Pickard, P.J. Hasnip, M.J. Probert, K. Refson, M. C. Payne, First principles methods using CASTEP, Z Krist-Cryst Mater. 220 (2005) 567–570.
[26] J. Perdew, J.A. Chevary, S.H. Vosko, K. Jackson, M. Pederson, D.J. Singh, C. Fiolhais, Atoms, molecules, solids, and surfaces: Applications of the generalized gradient approximation for exchange and correlation, Phys. Rev. B 46 (1992) 6671–6687.
[27] P.E. Blöchl, Projector augmented wave method, Phys. Rev. B 50 (24) (1994) 17953–17979.
[28] H.J. Monkhorst, J.D. Pack, Special points for Brillouin-zone integrations, Phys. Rev. B 13 (12) (1976) 5188–5192.
[29] S. Grimme, J. Antony, S. Ehrlich, H. Krieg, A consistent and accurate Ab initio parametrization of density functional dispersion correction (DFT-D) for the 94 elements H-Pu, Chem. Phys. 132 (2010), 154104.
[30] G. Kresse, J. Furthmüller, J. Hafner, Theory of the crystal structures of selenium and tellurium: the effect of generalized-gradient corrections to the local-density approximation, Phy. Rev. B 50 (1994) 13181.
[31] M. Chen, Z.H. Pan, X.J. Jin, Z. Chen, Y.T. Zhong, X.S. Wang, Y.C. Qiu, M.Q. Xu, W. S. Li, Y.G. Zhang, A highly integrated all-manganese battery with oxide nanoparticles supported on the cathode and anode by super-aligned carbon nanotubes, J. Mater. Chem. A 7 (2019) 4494–4504.
[32] Y. Pei, C.Y. Xu, Y.C. Xiao, Q. Chen, B. Huang, B. Li, S. Li, L. Zhen, G.Z. Cao, Phase transition induced synthesis of layered/spinel heterostructure with enhanced electrochemical properties, Adv. Funct. Mater. 27 (2017) 1604349.1-1604349.11.
[33] H. Guo, Z. Wei, K. Jia, B. Qiu, C. Yin, F. Meng, Q. Zhang, L. Gu, S. Han, Y. Liu, H. Zhao, W. Jiang, H. Cui, Y. Xia, Z. Liu, Abundant nanoscale defects to eliminate voltage decay in Li-rich cathode materials, Energy Stor. Mater. 16 (2019) 220–227.
[34] B. Wu, X. Yang, X. Jiang, Y. Zhang, H. Shu, P. Gao, L. Liu, X. Wang, Synchronous tailoring surface structure and chemical composition of Li-rich-layered oxide for high-energy Lithium-ion batteries, Adv. Funct. Mater. 28 (2018) 1803392.
[35] P. Liu, H. Zhang, W. He, T. Xiong, Y. Cheng, Q. Xie, Y. Ma, H. Zheng, L. Wang, Z. Z. Zhu, Y. Peng, L. Mai, D.L. Peng, Lithium deficiencies engineering in Li-rich layered oxide $Li_{1.098}Mn_{0.533}Ni_{0.113}Co_{0.138}O_2$ for high-stability cathode, J. Am. Chem. Soc 141 (2019) 10876–10882.
[36] Y.-P. Deng, Z.-W. Yin, Z.-G. Wu, S.-J. Zhang, F. Fu, T. Zhang, J.-T. Li, L. Huang, S.-G. Sun, Layered/spinel heterostructured and hierarchical micro/nanostructured Li-rich cathode materials with enhanced electrochemical properties for Li-ion batteries, ACS Appl. Mater. Interfaces 9 (25) (2017) 21065–21070.
[37] G. Xu, J. Li, Q. Xue, X. Ren, G. Yan, X. Wang, F. Kang, Enhanced oxygen reducibility of $0.5Li_2MnO_3{\cdot}0.5LiNi_{1/3}Co_{1/3}Mn_{1/3}O_2$ cathode material with mild acid treatment, J. Power Sources 248 (2014) 894–899.
[38] S.A.C. Carabineiro, S.S.T. Bastos, J.J.M. Órfão, M.F.R. Pereira, J.J. Delgado, J. L. Figueiredo, Carbon monoxide oxidation catalysed by exotemplated manganese oxides, Catal Letters 134 (3-4) (2010) 217–227.
[39] J. Zhang, R. Gao, L. Sun, Z. Li, H. Zhang, Z. Hu, X. Liu, Understanding the effect of an in situ generated and integrated spinel phase on a layered Li-rich cathode material using a non-stoichiometric strategy, Phys. Chem. Chem. Phys. 18 (36) (2016) 25711–25720.
[40] G. Cherkashinin, K. Nikolowski, H. Ehrenberg, S. Jacke, L. Dimesso, W. Jaegermann, The stability of the SEI layer, surface composition and the oxidation state of transition metals at the electrolyte–cathode interface impacted by the electrochemical cycling: X-ray photoelectron spectroscopy investigation, Phys. Chem. Chem. Phys. 14 (35) (2012) 12321.
[41] J. Chen, G.Q. Zou, W.T. Deng, Z.D. Huang, X. Gao, C. Liu, S.Y. Yin, H.Q. Liu, X. L. Deng, Y. Tian, J.Y. Li, C.W. Wang, D. Wang, H.W. Wu, L. Yang, H.S. Hou, X.B. Ji, Pseudo-bonding and electric-field harmony for Li-rich Mn-based oxide cathode, Adv. Funct. Mater. 30 (2020) 2004302.
[42] Y. Huang, K. Li, S. Li, Y. Lin, H. Liu, Y. Tong, Ultrathin Bi_2MoO_6 nanosheets for photocatalysis: performance enhancement by atomic interfacial engineering, Chemistry Select 3 (2018) 7423–7428.
[43] H. Yu, Y.-G. So, Y. Ren, T. Wu, G. Guo, R. Xiao, J. Lu, H. Li, Y. Yang, H. Zhou, R. Wang, K. Amine, Y. Ikuhara, Temperature-sensitive structure evolution of Lithium-manganese-rich layered oxides for Lithium-ion batteries, J. Am. Chem. Soc. 140 (45) (2018) 15279–15289.
[44] W.C. Bi, G.H. Gao, G.M. Wu, M. Atif, M.S. AlSalhi, G.Z. Cao, Sodium vanadate/PEDOT nanocables rich with oxygen vacancies for high energy conversion efficiency zinc ion batteries, Energy Stor. Mater. 40 (2021) 209–218.
[45] W.J. Jang, C.X. Zhang, Y.Z. Feng, B. Wei, L.B. Chen, R.F. Zhang, D.G. Ivey, P. Wang, W.F. Wei, Achieving high structure and voltage stability in cobalt-free Li-rich layered oxide cathodes via selective dual-cation doping, Energy Stor. Mater. 32 (2020) 37–45.
[46] Q. Li, H. Li, Q. Xia, Z. Hu, Y. Zhu, S. Yan, C. Ge, Q. Zhang, X. Wang, X. Shang, S. Fan, Y. Long, L. Gu, G.-X. Miao, G. Yu, J.S. Moodera, Extra storage capacity in transition metal oxide lithium-ion batteries revealed by in situ magnetometry, Nat Mater. 20 (1) (2021) 76–83.
[47] C. Yin, L.Y. Wan, B. Qiu, F. Wang, W. Jiang, H.F. Cui, J.M. Bai, S. Ehrlich, Z.N. Wei, Z.P. Liu, Boosting energy efficiency of li-rich layered oxide cathodes by tuning oxygen redox kinetics and reversibility, Energy Stor. Mater. 35 (2021) 388–399.
[48] W.Q. Tu, P. Xia, X.W. Zheng, C.C. Ye, M.Q. Xu, W.S. Li, Insight into the interaction between layered lithium-rich oxide and additive-containing electrolyte, J. Power Sources 341 (2017) 348–356.
[49] H. Yu, H. Kim, Y. Wang, P. He, D. Asakura, Y. Nakamura, H. Zhou, High-energy 'composite' layered manganese-rich cathode materials via controlling Li_2MnO_3 phase activation for lithium-ion batteries, Phys. Chem. Chem. Phys. 14 (2012) 6584.
[50] M. Chen, X.D. Xiang, D.R. Chen, Y.H. Liao, Q.M. Huang, W.S. Li, Polyethylene glycol-assisted synthesis of hierarchically porous layered lithium-rich oxide as cathode of lithium ion battery, J. Power Sources 279 (2015) 197–204.
[51] M. Chen, X. Jin, Z. Chen, Y. Zhong, Y. Liao, Y. Qiu, G. Cao, W. Li, A cross-like hierarchical porous lithium-rich layered oxide with (110)-oriented crystal planes as a high energy density cathode for lithium ion batteries, J. Mater. Chem. A 7 (21) (2019) 13120–13129.
[52] Y.I. Pei, Q. Chen, Y.-C. Xiao, L.I. Liu, C.-Y. Xu, L. Zhen, G. Henkelman, G. Cao, Understanding the phase transitions in spinel-layered-rock salt system: criterion for the rational design of llo/spinel nanocomposites, Nano Energy 40 (2017) 566–575.
[53] X.D. Zhang, J.L. Shi, J.Y. Liang, Y.X. Yin, J.N. Zhang, X.Q. Yu, Y.G. Guo, Suppressing surface lattice oxygen release of Li-rich cathode materials via heterostructured spinel $Li_4Mn_5O_{12}$ coating, Adv. Mater. 30 (2018) 1801751.
[54] Y.X. Jian, Z.F. Huang, J.D. Xing, L. Sun, Y.Z. Liu, P.Y. Gao, Phase stability, mechanical properties and electronic structures of tial binary compounds by first principles calculations-sciencedirect, Mater Chem Phys 221 (2019) 311–321.
[55] B. Li, H.J. Yan, J. Ma, P.R. Yu, D.G. Xia, W.F. Huang, W.S. Chu, Z.Y. Wu, Manipulating the electronic structure of Li-rich manganese-based oxide using polyanions: towards better electrochemical performance, Adv. Funct. Mater. 24 (2014) 5112–5118.
[56] N. Voronina, N. Yaqoob, H.J. Kim, K.-S. Lee, H.-D. Lim, H.-G. Jung, O. Guillon, P. Kaghazchi, S.-T. Myung, A new approach to stable cationic and anionic redox activity in O3-layered cathode for sodium-ion batteries, Adv. Energy Mater. 11 (25) (2021) 2100901.
[57] S. Tao, W. Huang, S. Chu, B. Qian, L. Liu, W. Xu, Dynamic structural evolution of oxygen vacancies in lithium rich layered composites cathodes for Li-ion batteries, Mater. Today Phys. 18 (2021) 100403.
[58] M.V. Reddy, G.V.S. Rao, B.V.R. Chowdari, Nano-$(V_{1/2}Sb_{1/2}Sn)O_4$: a high capacity, high rate anode material for Li-ion batteries, J. Mater. Chem. 21 (2011) 10003.
[59] R.Z. Yu, M.N. Banis, C.H. Wang, B. Wu, Y. Huang, S. Cao, J.J. Li, S. Jamil, X.T. Lin, F.P. Zhao, W.H. Lin, B.B. Chang, X.K. Yang, H. Huang, X.Y. Wang, X.L. Sun, Tailoring bulk Li^+ ion diffusion kinetics and surface lattice oxygen activity for high performance lithium-rich manganese-based layered oxides, Energy Stor. Mater. 37 (2021) 509–520.
[60] Q. Li, Y.I. Wang, X. Wang, X. Sun, J.-N. Zhang, X. Yu, H. Li, Investigations on the fundamental process of cathode electrolyte interphase formation and evolution of high-voltage cathodes, Acs Appl. Mater. Interfaces 12 (2) (2020) 2319–2326.
[61] L. Xu, Z. Sun, Y.U. Zhu, Y.U. Han, M. Wu, Y. Ma, Y.I. Huang, H. Zhang, Y. Chen, A Li-rich layered-spinel cathode material for high capacity and high rate lithium-ion batteries fabricated via a gas-solid reaction, Sci. China Mater. 63 (12) (2020) 2435–2442.
[62] J. Zhao, X.U. Zhang, Y. Liang, Z. Han, S. Liu, W. Chu, H. Yu, Interphase engineering by electrolyte additives for lithium-rich layered oxides: Advances and perspectives, ACS Energy Lett. 6 (7) (2021) 2552–2564.